Available online at www.sciencedirect.com
SCIENCE DIRECT®
International Journal of Heat and Mass Transfer 49 (2006) 3190–3210
International Journal of HEAT and MASS TRANSFER
www.elsevier.com/locate/ijhmt

Using oscillations to enhance heat transfer for a circular cylinder

Tait Sherman Pottebaum [a,*], Mory Gharib [b]

[a] Aerospace and Mechanical Engineering Department, University of Southern California, Los Angeles, CA 90089-1453, USA
[b] Graduate Aeronautical Laboratories, California Institute of Technology, 1200 E. California Blvd., Mail Code 205-45, Pasadena, CA 91125, USA

Received 26 February 2004; received in revised form 6 August 2004
Available online 11 April 2006

Abstract

An experimental investigation into the effects of transverse oscillations on the heat transfer from a circular cylinder in cross-flow was carried out. The cylinder's heat transfer coefficient was measured for a wide range of oscillation frequencies and amplitudes. Heat transfer enhancement was found to be strongly dependent on synchronization with harmonics of the natural shedding frequency, the cylinder wake mode, and the cylinder transverse velocity. For representative oscillation conditions, the velocity and temperature fields in the near wake were measured using digital particle image thermometry and velocimetry (DPIT/V). This revealed several mechanisms that explain the observed heat transfer enhancement.

1. Introduction

1.1. Motivation

It is evident from a review of the literature that transverse oscillations of a cylinder in cross-flow can result in significantly enhanced heat transfer under certain oscillation conditions. Also, it is clear that the wake structure is the connection between oscillations and heat transfer. However, the mechanism of this connection is not understood. Therefore, the goal of this study is to understand the mechanism through which transverse cylinder oscillations modify the heat transfer from the cylinder to the cross-flow. This goal is pursued by focusing on changes to the wake structure produced by oscillations and on how the wake structure in turn affects the heat transfer.

1.2. Circular cylinder wakes

The wake of a smooth, circular cylinder in a steady freestream flow can take several different forms. The form of the wake is primarily determined by the Reynolds number

$$Re = \frac{UD}{\nu},$$

where U is the freestream velocity, D is the cylinder diameter, and ν is the kinematic viscosity of the fluid. Changes in the form of the wake are related to stability transitions of various parts of the flow, such as the boundary layers or the free shear layers, if they exist, and these transitions occur at particular values of the Reynolds number.

For all Reynolds numbers, there is a stagnation point at the leading edge of the cylinder. From this stagnation point, boundary layers grow along the cylinder surface. For $Re > 5$, the boundary layers separate [1]. The vorticity in the free shear layers formed by the separated boundary layers rolls up into vortices in the wake. For Reynolds numbers greater than about 40, the Kármán Vortex Street is formed as vortices are shed from alternating sides of the cylinder. The frequency at which vortices are shed is known as the Strouhal frequency, f_{St}. The non-dimensional shedding frequency, or Strouhal number

$$St = \frac{f_{St}D}{U},$$

is a function of the Reynolds number. The vortex shedding from a cylinder is also influenced by the cylinder's aspect ratio [2].

* Corresponding author. Tel.: +213 821 5789; fax: +213 740 8071.
E-mail address: pottebau@usc.edu (T.S. Pottebaum).

0017-9310/$ - see front matter © 2006 Elsevier Ltd. All rights reserved.
doi:10.1016/j.ijheatmasstransfer.2006.01.037

Nomenclature

A	oscillation amplitude
B	number of phase-averaging bins
$C_{\Delta T}$	coefficient for the temperature difference between cylinder interior and surface
D	cylinder diameter
f	oscillation frequency
f^*	non-dimensional oscillation frequency
f_{St}	Strouhal, or natural shedding, frequency
g	acceleration due to gravity
h	heat transfer coefficient
k	thermal conductivity of the fluid
L	length of cylinder
N	number of snapshots
Nu	Nusselt number
P	power input to cylinder heating element
Pr	Prandtl number
Q	flow invariant from Perry and Fairlie
Re	Reynolds number
Ri	Richardson number
s	surface area of the cylinder
St	Strouhal number
T	temperature
u	streamwise component of velocity at a point
$\vec{u}$	velocity at a point
U	freestream speed
v	transverse component of velocity at a point
V_{rms}	root-mean-square transverse velocity of the cylinder
x	coordinate in the streamwise direction
y	coordinate in the transverse direction
z	coordinate along the cylinder axis

Greek symbols

α	thermal diffusivity
β	volumetric coefficient of thermal expansion
Γ	circulation
ϕ	phase angle of cylinder oscillation
η	vortex shedding angle
λ	wavelength of cylinder oscillations
λ_{f}	vortex formation length
ν	kinematic viscosity
θ	angular coordinate on the cylinder surface
ω	vorticity

Subscripts

0	non-oscillating cylinder
∞	freestream condition
b	phase-averaging bin index
mean	time average
n	snapshot index
rms	root-mean-square of fluctuations
surf	cylinder surface
tc	thermocouple

The wake of a cylinder that is oscillating sinusoidally in the direction transverse to the freestream direction can differ significantly from the wake of a non-oscillating cylinder. Williamson and Roshko [3] systematically studied the structure of wakes produced under different oscillation conditions. They identified several distinct distributions of vortices in the wake, which they referred to as wake modes.

Each wake mode corresponds to a particular number and grouping of vortices shed by the cylinder during one oscillation cycle and is designated by a combination of letters and numbers. The letter S indicates a single vortex, while the letter P indicates a pair of counter-rotating vortices with self-induced velocity away from the wake centerline. The $2S$ wake mode consists of two single vortices, one of each sign of vorticity, shed during each oscillation cycle, similar to the Kármán Vortex Street. In the wake mode designated $2P$, two vortex pairs are formed each cycle. The $P+S$ wake mode is asymmetric, with one vortex pair and one single vortex shed each cycle. The $2P+2S$ wake mode consists of two vortex pairs shed per cycle, with a single vortex shed between each pair. The notation $C(\,)$, where a wake mode is included inside of the parentheses, means that the indicated wake structure exists close to the cylinder but the vortices rapidly coalesce into larger structures downstream. Additional wake modes exist, but they are not relevant to the present study.

Williamson and Roshko identified the relevant non-dimensional parameters for determining the wake mode as the amplitude ratio, A/D, and the wavelength ratio, λ/D, where λ is the wavelength of the sinusoidal oscillations in a coordinate system moving with the freestream. For this study, a more convenient parameter is the frequency of oscillation, f. The frequency is non-dimensionalized as

$$f^* = \frac{fD}{U}.$$

This can be related to λ/D by

$$\frac{\lambda}{D} = \frac{U/f}{D} = \frac{U}{fD} = \frac{1}{f^*}.$$

Williamson and Roshko [3] also presented a map of the regions within the parameter space where the various wake modes occur. The exact position of the mode boundaries has been observed by the present authors to depend on Reynolds number, though the general shape and approximate locations remain consistent with the boundaries identified by Williamson and Roshko.

1.3. Heat transfer from non-oscillating cylinder

Heat transfer from stationary circular cylinders in cross-flow has been studied extensively and is considered well understood. This type of flow is thoroughly addressed in textbooks such as [4]. The heat transfer process is intimately connected to the boundary layer on the cylinder and the wake formation process.

At each point on the cylinder surface there is a local heat transfer coefficient that is a function of the local cylinder surface temperature and of the velocity and temperature profiles in the boundary layer at that location. Given the geometry of the flow, it is most natural to represent a location by its angle from the upstream stagnation point. The local heat transfer coefficient is defined as

$$h_\theta(\theta) \equiv \frac{\delta P(\theta)}{\Delta T(\theta) \cdot \delta s},$$

where δP is the power transferred across the surface element of area δs and ΔT is the difference between the surface temperature at that location and the freestream temperature. For engineering purposes, the average heat transfer coefficient over the entire cylinder, h, is of greater interest than the local heat transfer coefficients. The heat transfer coefficient is generally defined to allow the total heat flux across the surface to be determined from a relation of the form

$$P = hs\Delta T = h\pi DL\Delta T,$$

where s is the total surface area of the cylinder, P is the total power transferred across the surface, L is the cylinder's length, and ΔT represents the difference between the surface temperature and the freestream temperature. The particular definition of ΔT depends on the boundary condition at the surface for the specific case. The heat transfer coefficient is normalized by the cylinder diameter and the thermal conductivity of the fluid, k, to form the Nusselt number

$$Nu = \frac{hD}{k}.$$

In addition to the Reynolds number, the main parameter in determining the Nusselt number is the Prandtl number,

$$Pr = \frac{v}{\alpha},$$

where α is the thermal diffusivity of the fluid. The Prandtl number is the ratio of the diffusivity of momentum to the diffusivity of heat in the fluid.

Many empirical correlations with the Nusselt number exist. One widely used correlation is that of Zhukauskas [5]

$$Nu = 0.51Re^{0.5}Pr^{0.37}\left(\frac{Pr}{Pr_{\text{surf}}}\right)^{1/4}, \quad (1)$$

where Pr_{surf} is the Prandtl number at the cylinder surface temperature and all other parameters are evaluated at the freestream temperature. This correlation is valid in the range $Pr \leqslant 10$ and $40 < Re < 1000$. This correlation is for a cylinder with a uniform wall temperature (UWT) boundary condition, which corresponds to infinite azimuthal conduction. However, Mills [6] demonstrated that for external flows the average Nusselt numbers for UWT and uniform heat flux (UHF) boundary conditions are nearly equal, if they are properly defined. The UHF boundary condition corresponds to zero azimuthal conduction, so these two boundary conditions represent the extremes of the possible set of boundary conditions. This suggests that a suitably defined average Nusselt number for other boundary conditions will not differ substantially.

Another non-dimensional parameter that influences the Nusselt number is the Richardson number,

$$Ri = \frac{g\beta\Delta TD}{U^2},$$

where g is the acceleration due to gravity and β is the volumetric coefficient of thermal expansion for the fluid. The Richardson number represents the relative importance of free convection due to buoyancy compared to forced convection by the freestream flow.

The heat transfer from a cylinder in cross-flow has also been found to depend on the tunnel blockage ratio [5,7] (cylinder cross sectional area divided by the test section cross sectional area) and on the aspect ratio (L/D) of the cylinder [8,9].

1.4. Oscillating cylinder heat transfer

Heat transfer from transversely oscillating cylinders in cross-flow was first studied by Sreenivasan and Ramachandran [10]. For the small values of f^* in their study ($f^* \leqslant 0.07$), transverse oscillations had no effect on heat transfer, even at amplitude ratios up to 1.8.

Later work by various authors indicates that heat transfer is significantly enhanced when the cylinder is oscillated near the Strouhal frequency. Kezios and Prasanna [11] found that heat transfer was enhanced by about 20% for small amplitude ($0.02 < A/D < 0.075$) oscillations at the Strouhal frequency.

Saxena and Laird [12] reported that local heat transfer coefficients increase as the oscillation frequency approaches the Strouhal frequency. Heat transfer enhancement on the downstream half of the cylinder was consistently about 15% higher than for the leading half of the cylinder.

Cheng et al. [13] observed heat transfer enhancement of up to 34%. Enhancement near the Strouhal frequency was attributed to lock-on, or synchronization of the wake with the cylinder oscillations. High heat transfer coefficients at large amplitude ratios and high f^*, particularly for the highest Reynolds numbers examined, were attributed to a vague "turbulence effect".

Gau et al. [14] reported that heat transfer is significantly enhanced at 1 and 3 times the Strouhal frequency, and the

most significant enhancement occurs near the trailing edge of the cylinder for these cases.

Park and Gharib [15] found that heat transfer was significantly enhanced at frequencies corresponding to 1, 2 and 3 times the Strouhal frequency. Using digital particle image thermometry/velocimetry, Park and Gharib were able to show that the heat transfer enhancement was correlated with a shortening of the vortex roll-up distance.

Two common trends in the above literature suggest a relationship between the wake structure and the heat transfer. First, enhanced heat transfer is observed for oscillations at the natural vortex shedding frequency of the stationary cylinder and at some of its harmonics. Second, for oscillation conditions with significant heat transfer enhancement, the largest increases in local heat transfer coefficient occur on the trailing half of the cylinder, where the influence of the trailing vortices is strongest. These facts imply that the vortex roll-up process is directly involved in determining the cylinder heat transfer coefficient. It is therefore reasonable to suspect that the heat transfer coefficient for an oscillating cylinder will be correlated with the wake mode.

While a reasonable portion of the $(1/f^*, A/D)$-plane has been investigated by these authors, it has been in many small segments. Different information is available for each study, and it is difficult to compare results quantitatively because the methods used to determine the Nusselt number have varied widely. The details of the setups—such as Reynolds number, aspect ratio and Prandtl number—have also varied. Therefore, a consistent picture of the dependence of the heat transfer coefficient on the oscillation parameters known to determine the wake mode does not exist.

1.5. Digital particle image thermometry and velocimetry

Digital particle image thermometry and velocimetry (DPIT/V) is a combination of two techniques that allows the temperature field and the velocity field to be measured simultaneously in a thin cross section of a flow. Digital particle image velocimetry (DPIV) is a technique for determining the velocity field from consecutive images of particles suspended in a flow. Digital particle image thermometry (DPIT) refers to the extraction of temperature field information from the color of thermochromic liquid crystal (TLC) particles, which change their reflected wavelength with temperature. DPIT/V combines these two techniques by using the TLC particles as both temperature indicators and flow tracers.

DPIT/V is carried out by seeding a flow with TLC particles, illuminating a cross section with a sheet of white light, and digitally recording color images of the illuminated particles. The intensity field of the images, i.e., the black-and-white image left when color information is removed, is used to determine the velocity field through standard DPIV algorithms. The color information in the images is used to determine the temperature field.

DPIV is the digital version of the particle image velocimetry technique and was first used by Willert and Gharib [16]. DPIV processing techniques have progressed since this initial implementation, but the central idea remains unchanged. Cross-correlations of small windows in consecutive images produce displacement estimates, which are converted to velocities using the known time separation between images. A comparison of widely used DPIV processing techniques can be found in McKenna and McGillis [17].

DPIT depends upon the property of TLC that it selectively reflects light of a particular wavelength. The TLC acts as a Bragg scattering volume grating with a temperature dependant pitch. The apparent color of the TLC therefore depends on the temperature and on the angle between the incident light and the observer. Because the relationship between color and temperature is sensitive to chemical composition and to the optical arrangement, it is necessary to calibrate TLC particles for use in experiments. A complete discussion of the optical and chemical properties of TLC can be found in Parsley [18].

TLC has been used extensively for measuring temperature on surfaces. The first reported use of TLC applied to a surface for fluid mechanics research was in a qualitative study by Klein [19]. More recently, TLC has been used to seed fluid flows in order the measure the temperature field within the flow. Rhee et al. [20] pioneered this use, though their results were only qualitative. The DPIT technique in its present form was introduced by Dabiri and Gharib [21] and was later used to investigate the wakes of heated cylinders by Park et al. [22].

The quantitative measurement of temperature fields using TLC has advanced considerably in recent years. Park [23] presents a review of various color decomposition schemes used for TLC calibration. According to Park et al. [22], the uncertainty in temperature for individual TLC particles is 5–20% of the useful temperature range. A range of uncertainties is used because the calibration curve is non-linear, so the uncertainty varies over the useful temperature range. For 32×32 pixel averaging windows, this uncertainty is reduced to 2–10%.

2. Experimental details

2.1. Experimental approach

The approach taken in this set of experiments involved two stages. In the first stage, a parameter space survey was conducted over a large region of the frequency–amplitude plane. The heat transfer coefficient for the oscillating cylinder was determined for each test point. Data from the parameter space survey, combined with published information about wake mode regions, was used to identify relationships between the oscillation parameters and heat transfer enhancement.

The parameter survey data was also used to select particular cases for further investigation in order to

understand the mechanisms of heat transfer enhancement. These cases were studied using DPIT/V, allowing the velocity and temperature fields in a cross section of the flow to be measured simultaneously.

2.2. General setup

The experiments described in this paper were carried out in the GALCIT heat transfer water tunnel. The freestream temperature in this facility can be controlled to within ±0.02 °C over a range between ambient room temperature and 60 °C. Fig. 1 shows a diagram of the water tunnel and the arrangement of other elements. The test section is 152 mm wide, 580 mm long, and has a maximum height of 160 mm. For this study, an upper wall was located 133 mm above the bottom of the test section. The water tunnel was operated at a speed of 64.0 ± 1.0 mm/s for these experiments. The freestream temperature, T_∞, was set at 25.8 °C, and the properties of water at 25.8 °C were used as characteristic values to form dimensionless quantities.

The cylinder used in this study was a 9.42 mm diameter custom cartridge heater manufactured by Watlow. It consisted of a thin coil of high resistivity wire (80% Ni, 20% Cr) surrounded by compacted magnesium oxide insulator and encased in an Incolloy® 800 (a stainless steel alloy) sheath. The cylinder had a 127 mm heated length, with a 25 mm unheated extension at the end with the electrical connections, and a 6 mm unheated section at the other end. The cylinder also contained a type-J thermocouple embedded at the center of the heated length along the cylinder axis. When mounted in the test section, the cylinder had an aspect ratio of 14.2 and a blockage ratio of 0.0620. The aspect ratio was sufficiently large and the blockage ratio sufficiently small that the non-oscillating cylinder results are independent of these parameters [9].

For the experiments, the cylinder was suspended vertically in the test section. A slot in the upper wall allowed the cylinder to pass through. The full heated length of the cylinder was in the test section, and the unheated lead end was used to mount the cylinder on the oscillation mechanism using an insulated bracket.

Heating power was provided to the cylinder by a variable-voltage DC power supply (Kepco BOP 50-4M). A nominal input power of 63.8 W was used. The actual power input was monitored by independently measuring the current through and the voltage across the cylinder heating wire. This level of power input results in Richardson numbers below 0.054.

The cylinder was oscillated sinusoidally in the direction transverse to the flow by a closed loop motion control system. The major components of the system were a programmable motion controller (Delta Tau mini-PMAC), a linear voice coil actuator (BEI Kimco LA25-42000A), and a linear optical encoder (RSF Electronics MSA 6704). Motion control programs were developed for the controller specifying sinusoidal profiles of unit amplitude for various oscillation periods. Profiles were specified such that the time between successive points on the profile never exceeded

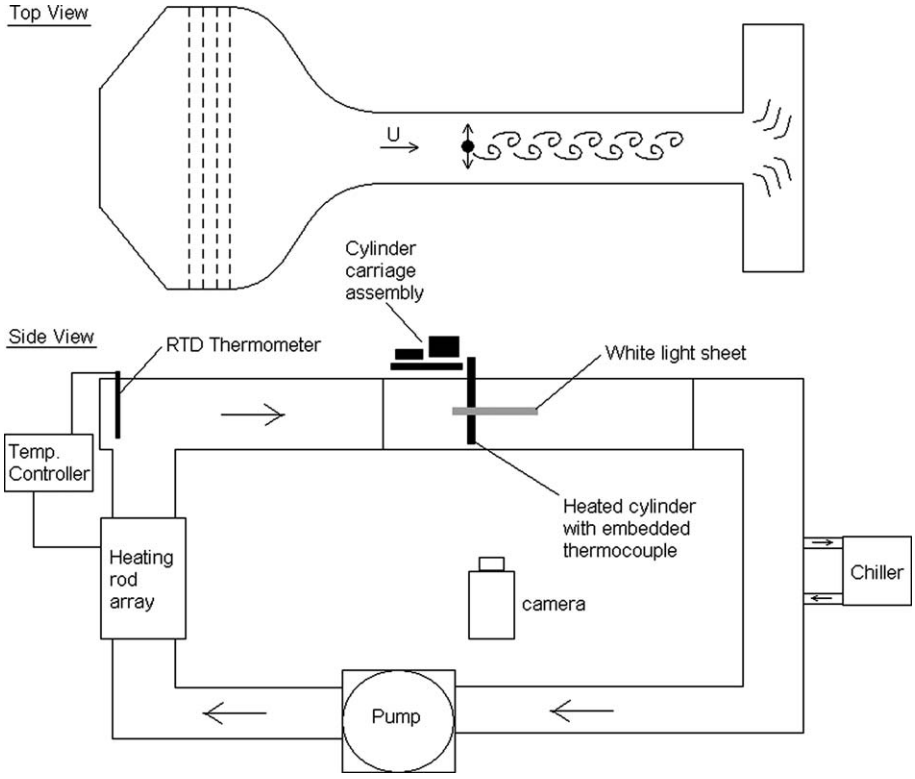

Fig. 1. Experimental setup.

1.5% of the oscillation period. The oscillation amplitude was set by changing the number of encoder counts defined as the unit of distance. The linear optical encoder had a resolution of 10 μm, corresponding to 2.1% of the smallest oscillation amplitude used. The encoder was attached directly to the cylinder carriage to avoid any scaling or hysteresis problems associated with linkages. The cylinder carriage assembly was anchored to the building structure to minimize vibrations and was suspended above the test section of the water tunnel.

2.3. Determination of heat transfer coefficient

As discussed in Section 1.3, it is necessary to define the heat transfer coefficient for the cylinder in a manner consistent with the boundary conditions at the cylinder surface. In this study, the boundary condition is neither UWT nor UHF. Rather, the total heat flux is controlled and the cylinder is allowed to reach a steady distribution of heat flux and wall temperature over the surface. The heat transfer coefficient is therefore defined, similar to the UHF case, as

$$h \equiv \frac{P}{\overline{\Delta T} \cdot s} = \frac{P}{\overline{\Delta T} \cdot \pi DL},$$

where $\overline{\Delta T}$ is the difference between the spatial average of the surface temperature and the freestream temperature.

Since the temperature is measured only at the cylinder axis, it is not possible to determine the true average surface temperature. Instead, an estimate of the average cylinder surface temperature was determined from the temperature at the cylinder core—as measured by the embedded thermocouple—using a steady, one-dimensional model of heat transfer inside the cylinder. The model used in this study is similar to that used by Park and Gharib [15]. This method produces results consistent with published values of heat transfer coefficient for both stationary and oscillating cylinders, but is limited by the assumption that the heat transfer coefficient is steady.

The details of the one-dimensional axisymmetric model derivation can be found in [24]. The resulting expression for the cylinder heat transfer coefficient is

$$h = \left(\frac{\pi DL}{P}(T_{\mathrm{tc}} - T_\infty) + C_{\Delta T}\right)^{-1}, \tag{2}$$

where T_{tc} is the temperature of the thermocouple and $C_{\Delta T}$ is a constant related to the internal structure and material properties of the cylinder. The impact of the axisymmetric assumption was analyzed by comparison with a two-dimensional model using local heat transfer coefficient data reported in [14] for a stationary cylinder, which is assumed to be the case which is furthest from axisymmetric. The heat transfer coefficient obtained from the one-dimensional model differed by only 1.9% from that obtained from the two-dimensional model.

Rewriting Eq. (2) as

$$C_{\Delta T} = \frac{1}{h} - \frac{\pi DL}{P}(T_{\mathrm{tc}} - T_\infty), \tag{3}$$

it is evident that the constant $C_{\Delta T}$ can be found by calibration if known values of the heat transfer coefficient can be produced. This was accomplished by subjecting the non-oscillating heated cylinder to 13 different freestream velocities. The empirical correlation given in Eq. (1) was used to determine the "actual" heat transfer coefficient. The values given by Eq. (3) for each freestream velocity were then averaged to form the best estimate of $C_{\Delta T}$. Eq. (1) requires the cylinder surface temperature to be estimated, which requires a value of $C_{\Delta T}$, so an iterative procedure was used until the best estimate for $C_{\Delta T}$ converged. By using a calibration to determine the value for $C_{\Delta T}$, some of the details of the actual system that were ignored in the model, such as temperature variations in the axial and angular directions, may be accounted for while retaining the linear relationship between power input and temperature difference. However, the best estimate of $C_{\Delta T}$ differed from the value calculated from the dimensions and material properties of the cylinder by only 8%, which is less than the standard deviation in the individual estimates of $C_{\Delta T}$.

The uncertainty in the heat transfer coefficient due to bias or systematic error is given by

$$\frac{\delta_h}{h} = (hC_{\Delta T} - 1)\left[\frac{\delta_{T_{\mathrm{tc}}} - \delta_{T_\infty}}{T_{\mathrm{tc}} - T_\infty} - \frac{\delta_P}{P} + \frac{\delta_D}{D} + \frac{\delta_L}{L}\right] - h\delta_{C_{\Delta T}},$$

where $\delta_{()}$ indicates the uncertainty in the subscripted quantity. Using appropriate values for the various uncertainties, it is apparent that uncertainty in the value of $C_{\Delta T}$ is the dominant source of systematic uncertainty in the measurement of the heat transfer coefficient.

For the non-oscillating cylinder, the standard deviation in the estimates of $C_{\Delta T}$ leads to a 10% uncertainty in the heat transfer coefficient. The relative uncertainty due to $C_{\Delta T}$ increases linearly with h, so this can be a very large source of error for large heat transfer coefficients. While the magnitude of the heat transfer coefficients may suffer from this source of error, any trends observed are not affected.

The relative uncertainty in the heat transfer coefficient due to random errors is given by

$$\overline{\left(\frac{\delta_h}{h}\right)^2} = (1 - hC_{\Delta T})^2\left[\frac{\overline{\delta_{T_{\mathrm{tc}}}^2} + \overline{\delta_{T_\infty}^2}}{(T_{\mathrm{tc}} - T_\infty)^2} + \overline{\left(\frac{\delta_P}{P}\right)^2}\right], \tag{4}$$

where an over bar indicates the average or most-likely value of the quantity. As with the systematic uncertainty, the random uncertainty depends significantly on the heat transfer coefficient itself. The term $(1 - hC_{\Delta T})^2$ increases with h, amplifying the uncertainty for large values of h. In addition, the temperature uncertainties are weighted by the inverse of the measured temperature difference, which decreases as h increases.

Uncertainty in the thermocouple temperature measurement is the dominant source of random error. Filtering

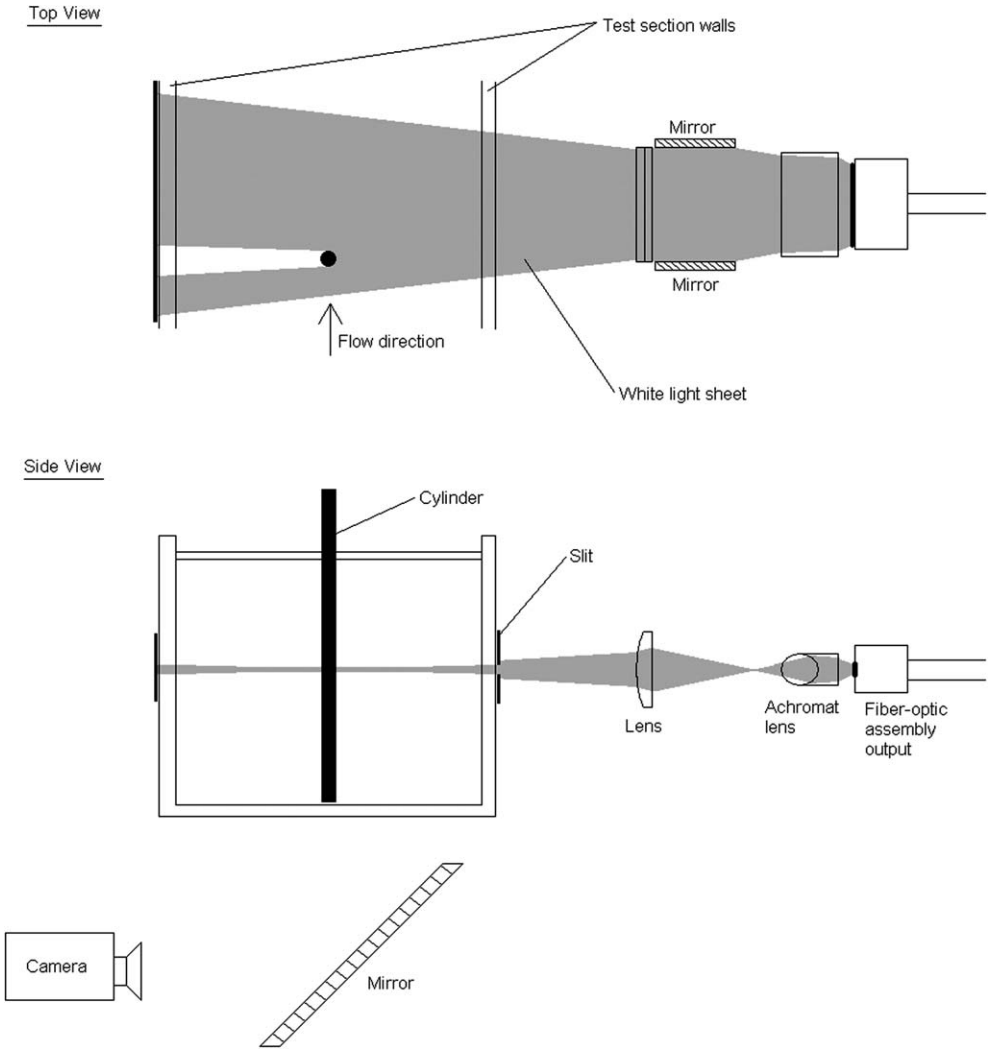

Fig. 2. Illumination and viewing setup for DPIT/V.

and averaging over a large number of samples eliminates the majority of the noise in the thermocouple signal, but the thermocouple itself is an inherently imprecise device. The uncertainty in the measured temperature is estimated to be ±0.1 °C. Applying Eq. (4), this corresponds to a relative uncertainty in h of 1% when $h \approx h_0$ and 7% when $h \approx 3h_0$. This level of uncertainty is consistent with an observed 2% maximum variation in the heat transfer coefficient from repeated measurements of the non-oscillating cylinder case.

2.4. DPIT/V setup and processing

For DPIT/V, the water tunnel was seeded with 40 μm diameter encapsulated TLC particles (Hallcrest BM/R26C20W/S33). The thermal time constant for these particles is estimated to be 4 ms [21], which is much shorter than the characteristic timescales in the flow. Under the conditions used in the study (approximately 90° between illumination and viewing directions), the useful temperature range is about 2 °C, with the low temperature start at 25.4 °C. A diagram of the illumination and imaging setup is shown in Fig. 2.

The particles were illuminated by a horizontal sheet of pulsed white light at the mid-plane of the test section. The light sheet was formed using a white light source consisting of two xenon strobes coupled by a fiber-optic assembly. At the center of the test section, the light sheet had a thickness of 5 mm. The separation time between pulses of the light sheet for each image pair was set such that the vector sum of the freestream velocity and the peak cylinder transverse velocity corresponded to a displacement of approximately 4 pixels.

The illuminated particles were imaged using a color, progressive scan CCD camera (Sony DXC-9000) at the standard NTSC video rate of 29.97 frames per second. The camera was located 1.3 m from the illuminated plane, and the field of view was 67 mm × 51 mm with the larger dimension in the streamwise direction. The resulting images were recorded directly to computer hard disk in

real time using an analog frame grabber and video capture software. Synchronization of the light pulses to the video frames was accomplished using a National Instruments PC-TIO-10 timing card.

The cylinder used in this study was not transparent, so there was a shadow in every image. No useful velocity or temperature information could be extracted from the shadow region. In addition, derivative and integral quantities, such as vorticity, circulation, or the temperature gradient, could not be determined for points bordering the shadow region or for areas or paths that include the shadow region.

The intensity field of the recorded images was used as the input for standard DPIV processing algorithms to determine the velocity field. DPIV processing was carried out using 32 pixel by 32 pixel interrogation windows with 50% overlap. Window shifting was used to reduce errors associated with in-plane particle loss. The CCD resolution and out-of-plane particle loss are the main remaining sources of error. Overall, the measured velocities have relative uncertainties of approximately 1.5%.

The intensity field was also used to determine the phase of motion of the cylinder for oscillating cases. The cylinder position was first estimated by measuring the extent of the cylinder's shadow in each image. Position estimates for each pair of images were then averaged together. Using the known cylinder oscillation period for a particular case and the time between image pairs, a sine wave at the proper frequency,

$$y = A\sin(2\pi ft + \phi_i),$$

where ϕ_i is the phase at $t = 0$, was fit to the time series of position estimates in order to determine the phase of each image pair, ϕ.

Temperature field data was extracted from the color content of the DPIT/V images using a new localized calibration scheme, inspired by Sabatino et al. [25], intended to account for the effects of viewing angle on the apparent color of the TLC particles. The red–green–blue (RGB) color data for each image was converted to the hue-saturation-intensity (HSI) color scheme, and the hue angle was used as the indicator of temperature. The conversion from RGB to HSI used the relationships

$$\begin{bmatrix} v_1 \\ v_2 \\ I \end{bmatrix} = \begin{bmatrix} 1 & -1/2 & -1/2 \\ 0 & \sqrt{3}/2 & -\sqrt{3}/2 \\ 1/3 & 1/3 & 1/3 \end{bmatrix} \begin{bmatrix} R \\ G \\ B \end{bmatrix},$$

$$H = \tan^{-1}(v_2/v_1),$$

$$S = \sqrt{v_1^2 + v_2^2}.$$

The images were divided into 16 pixel by 16 pixel color-averaging windows, and each window was calibrated separately. After applying intensity and saturation thresholds, the hues of all non-black pixels in a window were averaged to define the hue for that window. The hue was then converted to temperature using a lookup table of the calibration hue values and linear interpolation between calibration temperatures. To determine the temperature on the same grid as the DPIV data, the temperature of 2 by 2 groups of temperature widows were averaged together, weighted by the number of non-black pixels in each window. The temperature fields of the two images in each image pair were then averaged together with equal weight to produce the temperature field snapshots corresponding to the DPIV velocity snapshots.

Calibration images were recorded using the same setup as the data images. The only change in the setup was that the cylinder was removed from the test section for the calibration images. One hundred images of the seeded flow were recorded at each calibration temperature in approximately 0.1 °C increments over the entire active range of the TLC particles. Hue values for the calibration images were determined in the same manner as for the data images.

It was found that the useful range of the TLC particles was significantly smaller in the portion of the field-of-view upstream of the cylinder than in the downstream portion. Therefore, temperature data was only considered reliable in the downstream portion of the flow.

With the implementation described here, DPIT/V is capable of measuring temperature differences of approximately 0.1 °C over a range of about 1 °C. Smaller temperature differences cannot be resolved and will likely be overwhelmed by noise.

2.5. Parameter space survey procedure

For the parameter space survey, a single data acquisition run consisted of a large set of amplitude–frequency combinations to be performed. Control of the cylinder oscillations and acquisition of data was automated using a program written in LabVIEW to enable the large number of cases to be considered in a reasonable period of time.

For each case in a run, there was a delay of at least 30 s after the cylinder motion was started to allow the cylinder to reach its new equilibrium temperature. Following the delay, voltage data from the embedded thermocouple was recorded for 200 s at a rate of 20 samples per second. When data acquisition was completed, the cylinder motion was stopped and a delay of 20 s was imposed before beginning the next case. This delay allowed any wake structures generated by the cylinder oscillations to leave the test section so that they did not affect the next case.

The freestream temperature, cylinder power input and other data about the operating conditions were monitored and recorded throughout each run. Following the run, these values were used in the data processing to account for any variations in the conditions.

2.6. DPIT/V procedures

Before being added to the water tunnel, the TLC particles used for DPIT/V were heated past their blue clearing temperature. The calibration curve of the TLC can shift after the particles are exposed to temperatures above the

blue clearing point [25]. If this were to happen during the experiment, the calibration would be incorrect. Therefore, the particles were pre-heated so that any shift took place before the experiments began. Approximately 40 mL of TLC slurry was diluted in 1000 mL of de-ionized water. The particles were then heated and mixed using a hot plate/stirrer until the blue clearing temperature was exceeded. This process took about 25 min.

The TLC particles were then added to the water tunnel through a sieve with 75 μm openings. This removed large particles or clumps of particles that would either fail to follow the flow or produce over-saturated images. The resulting particle loading of the tunnel was about 0.02% by volume. Approximately 30 min, or 15 tunnel re-circulation times, was allowed for the TLC particles to mix with the water in the tunnel. This time also allowed for an equilibrium amount of water to penetrate the protein encapsulation of the TLC particles.

Acquisition of DPIT/V and thermocouple data was automated, using a modified version of the LabVIEW program used for the parameter space survey. Code was included so that the program triggered the light sheet pulsing and the acquisition of video images. This resulted in synchronized DPIT/V and thermocouple data for each case. This automation allowed the set of cases to be investigated in a period of time over which the TLC color-temperature relationship remained fairly constant. DPIT calibration data was acquired at the end of each run.

For the purpose of analyzing wake structure and heat transport, the velocity and temperature field snapshots

Table 1
Cases investigated with DPIT/V

Case	$1/f^*$	f^*	A/D	Nu/Nu_0	Mode
0	~4.76	~0.21	0.00	1.00	
1	0.92	1.082	0.10	0.96	*NS*
2	1.07	0.932	0.85	8.22	*C*(2*S*)
3	1.37	0.729	0.70	4.88	*C*(2*S*)
4	1.37	0.729	0.80	5.72	*C*(2*S*)
5	1.81	0.553	0.10	1.20	*C*(2*S*)
6	1.96	0.511	0.85	3.32	*C*(2*S*)
7	2.10	0.476	0.30	1.47	*C*(2*S*)
8	2.54	0.394	0.10	0.99	*C*(2*S*)
9	2.68	0.373	0.20	1.02	*C*(2*S*)
10	2.68	0.373	0.90	2.22	*C*(*P* + *S*)
11	2.98	0.336	0.30	1.23	*C*(2*S*)
12	3.13	0.320	0.45	1.37	*C*(2*S*)
13	3.71	0.270	1.00	1.84	2*P*
14	3.99	0.250	0.20	1.13	2*S*
15	3.99	0.250	0.50	1.48	2*S*/*C*(2*S*)
16	4.29	0.233	0.60	1.58	2*S*
17	4.59	0.218	0.25	1.28	2*S*
18	4.59	0.218	0.90	1.67	2*P*
19	4.73	0.211	0.10	1.17	2*S*
20	5.18	0.193	0.30	1.38	2*S*
21	5.75	0.174	0.55	1.35	2*S*/2*P*
22	5.75	0.174	0.65	1.30	2*P*
23	5.90	0.169	0.30	1.08	2*P*
24	6.20	0.161	0.55	1.18	2*P*
25	7.80	0.128	0.30	1.01	2*P*
26	7.80	0.128	0.90	1.23	2*P*
27	9.75	0.103	0.90	1.11	2*P*
28	10.24	0.098	0.30	1.00	*NS* or 4*S*
29	11.70	0.085	0.60	1.00	2*P*
30	15.11	0.066	0.20	1.00	6*S*

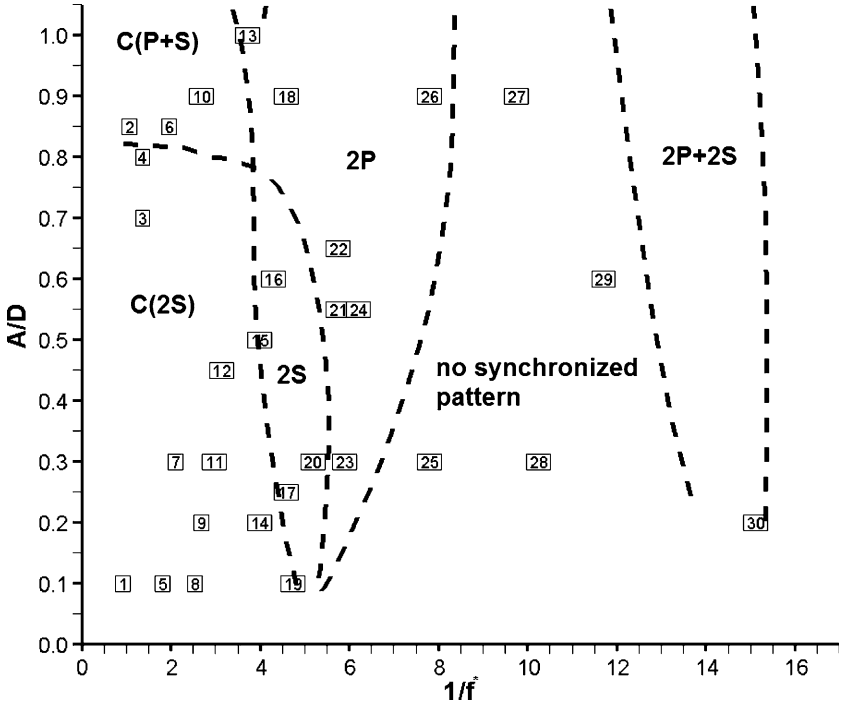

Fig. 3. Cases investigated using DPIV/T, as indicated by numbers; the Williamson and Roshko [3] wake mode regions are labeled, with the boundaries indicated by dashed lines.

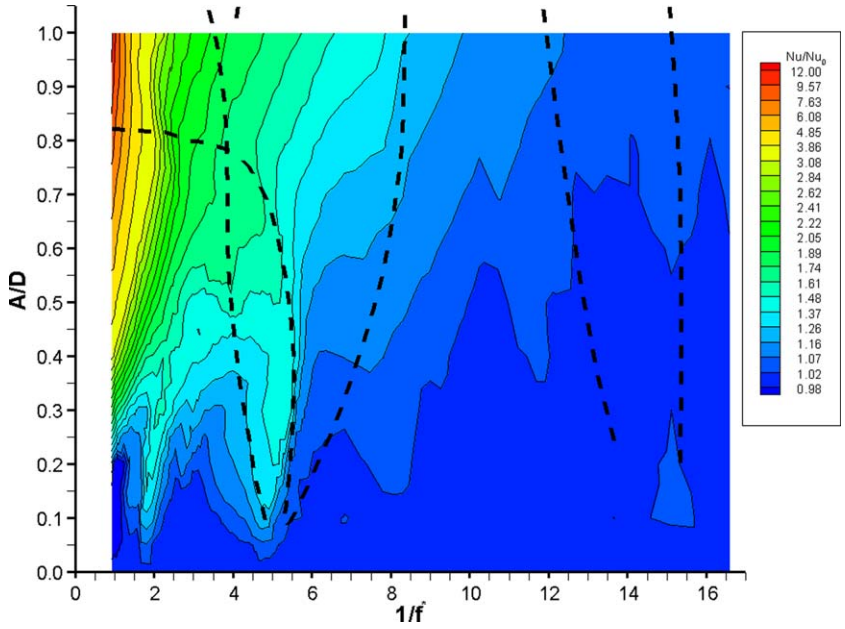

Fig. 4. Normalized Nusselt number as a function of oscillation parameters; Williamson and Roshko [3] wake mode boundaries are shown as dashed lines.

obtained using DPIT/V were combined to form phase-averaged, mean, and root-mean-square (rms) fields. For phase averaging, individual snapshots were grouped into bins by the phase of the cylinder motion. The mean and rms of each bin was computed as

$$\langle q_b \rangle \equiv \frac{1}{N_b} \sum_n q_{bn},$$

$$q^*_{bn} \equiv q_{bn} - \langle q_b \rangle,$$

$$q_{b,rms} \equiv \sqrt{\frac{1}{N_b} \sum_n q^{*2}_{bn}} = \sqrt{\frac{1}{N_b} \sum_n q^2_{bn} - \langle q_b \rangle^2},$$

where q is a flow quantity (velocity component, temperature or vorticity), b is the index indicating the phase bin, N_b is the number of snapshots in bin b, and n is the index of snapshots in bin b. In most cases, the cylinder motion was divided into 16 phase bins over one oscillation period. In cases where the flow was expected to synchronize with the cylinder motion over multiple oscillation cycles, such as at Strouhal frequency harmonics, the phase groupings extended over the appropriate number of cycles, with 16 bins per cycle.

The mean and rms fields are intended to represent the flow with each phase of the oscillation cycle equally represented. They are therefore defined as

$$q_{\text{mean}} \equiv \frac{1}{B} \sum_b \langle q_b \rangle,$$

$$q_{\text{rms}} \equiv \sqrt{\frac{1}{B} \sum_b \left(q^2_{b,\text{rms}} + \langle q_b \rangle^2 \right) - q^2_{\text{mean}}},$$

where B is the number of phase bins.

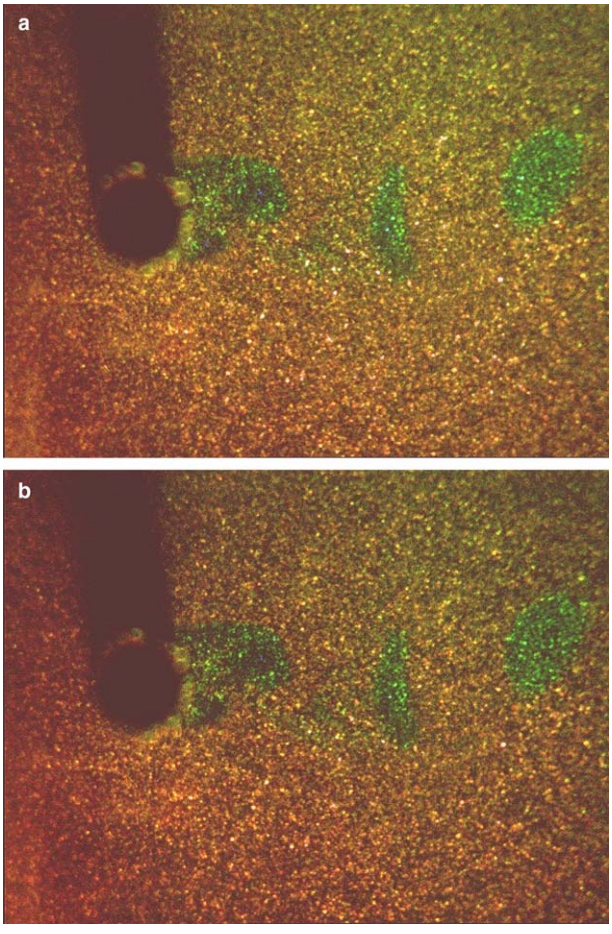

Fig. 5. Sample image pair from case 19; color equalized and brightness increased to improve print quality.

2.7. Experimental conditions

Amplitude ratios up to $A/D = 1$ and non-dimensional frequencies in the range $0.061 \leqslant f^* \leqslant 1.08$ were considered. The freestream velocity was 64.0 ± 1.0 mm/s, resulting in a Reynolds number of 687. The Strouhal number has a value of 0.21 at this Reynolds number [26]. For the non-oscillating cylinder, the wake at this Reynolds number is

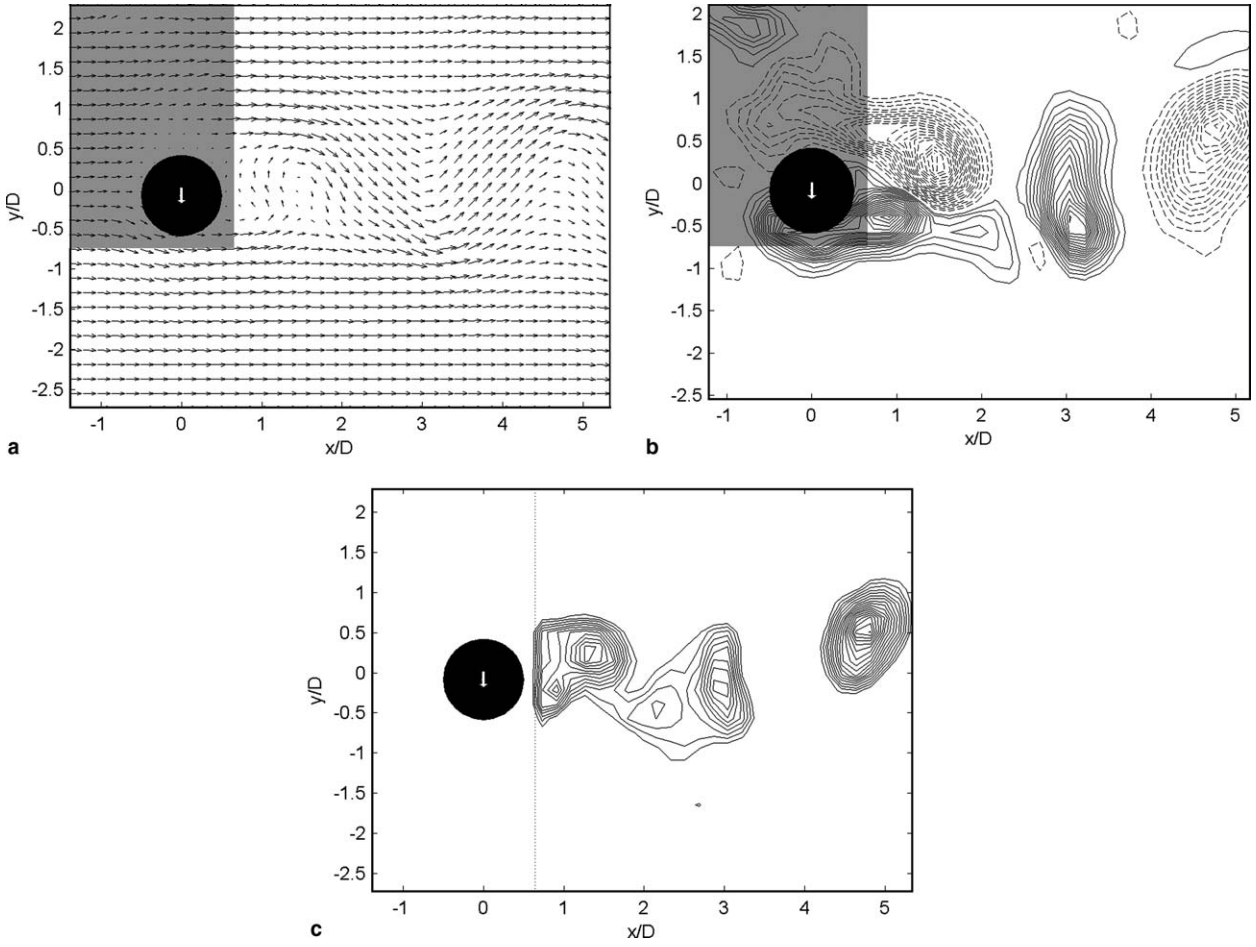

Fig. 6. Data extracted from pair of images in Fig. 5 (a) velocity (b) normalized vorticity $[\omega D/U]$ contour spacing 0.2, positive contours solid, negative contours dashed (c) normalized temperature $[(T - T_\infty)/(T_{\text{surf}} - T_\infty)]$ minimum contour 0.015, contour spacing 0.005.

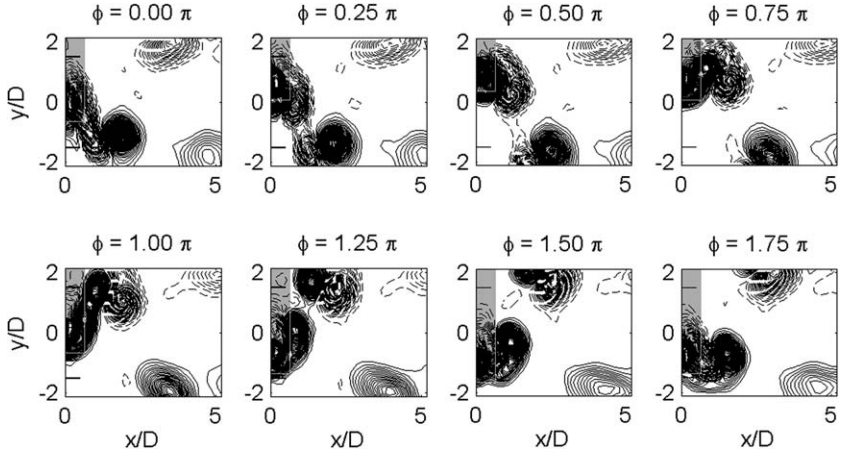

Fig. 7. Phase-averaged vorticity for case 13.

three-dimensional. For the oscillating cases, however, the cylinder motion forces the vortices to shed parallel to the cylinder [27]. Data was obtained at 1070 distinct oscillation conditions, including 64 different frequencies and 20 amplitudes, in addition to the non-oscillating case.

The nominal input power to the cylinder was 63.8 W and the freestream temperature (T_∞) was approximately 25.8 °C for all cases. Over the full set of cases, the input power and the freestream temperature differed from the nominal values by up to ±0.1 W and ±0.1 °C due to slow drift in the equipment. However, the power input and freestream temperature for each case were steady to within ±0.01 W and ±0.02 °C over the duration of that case.

A total of 31 cases were investigated in the DPIT/V experiments on wake structure, including the non-oscillating case. The specific cases chosen are indicated in Table 1 and in Fig. 3. The non-oscillating case is not shown in Fig. 3. In order to distinguish between cases, each case was assigned a number. Case 0 is the non-oscillating case. All oscillating cases are numbered in order of decreasing frequency, i.e., from left to right in Fig. 3. For cases with the same frequency, the smaller amplitude case has the lower number. Fig. 3 also shows the regions associated with the various wake modes [3].

3. Results

The results of the parameter space survey are shown in Fig. 4 as contours of the Nusselt number (Nu) normalized by the Nusselt number of the non-oscillating cylinder (Nu_0). The contour levels bracketing unity were selected to indicate those values that are measurably different than one, based upon the repeatability of the measurements. Other contour levels are spaced exponentially. The wake mode boundaries identified by Williamson and Roshko [3] are superimposed on the contour plot as dashed black lines.

A typical pair of DPIT/V data images, taken from case 19, is shown in Fig. 5. The instantaneous normalized velocity, vorticity and temperature fields corresponding to this

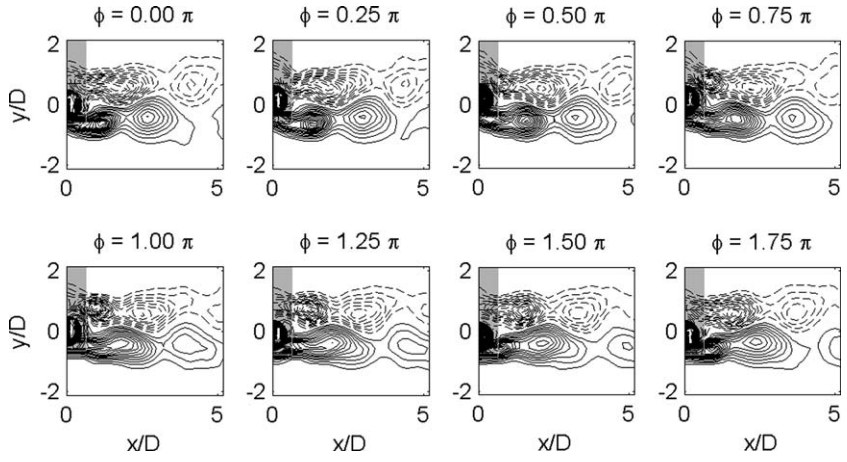

Fig. 8. Phase-averaged vorticity for case 14.

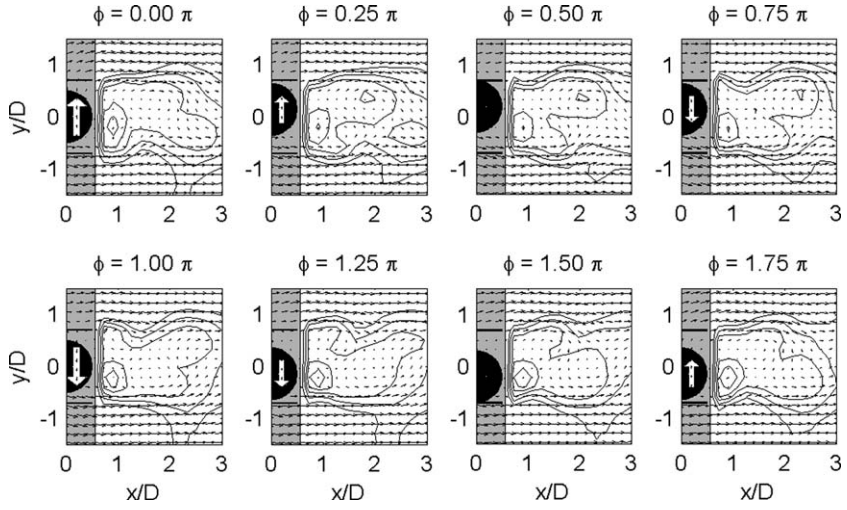

Fig. 9. Phase-averaged velocity and temperature for case 14.

image pair are shown in Fig. 6. The gray rectangle in the velocity and vorticity plots indicates data that is not reliable because of the cylinder's image and shadow. In the plot of the temperature field, the dotted line indicates the streamwise location upstream of which the temperature range of the TLC particles was not sufficiently large to be useful.

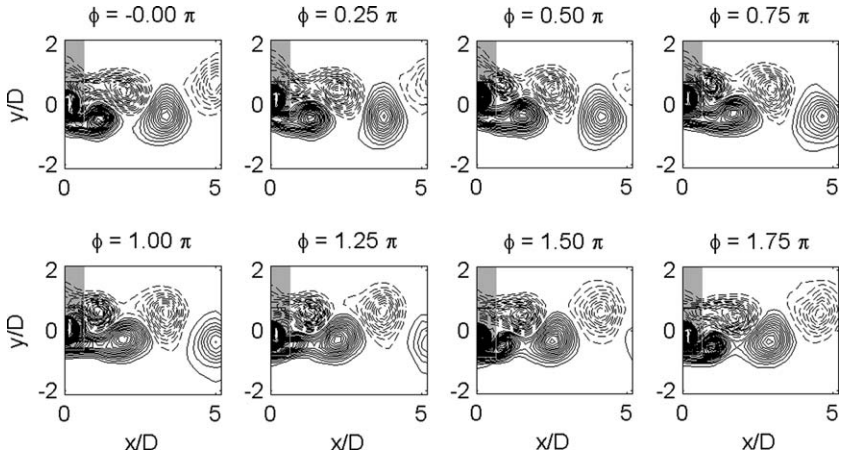

Fig. 10. Phase-averaged vorticity for case 17.

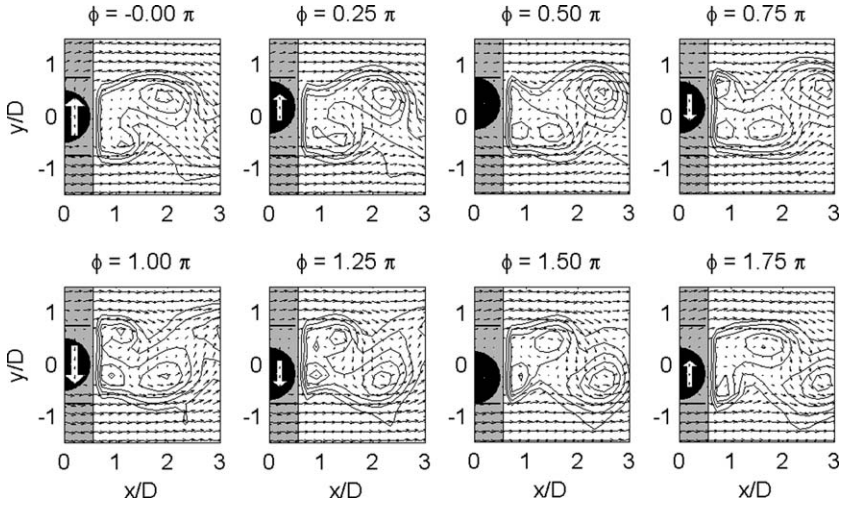

Fig. 11. Phase-averaged velocity and temperature for case 17.

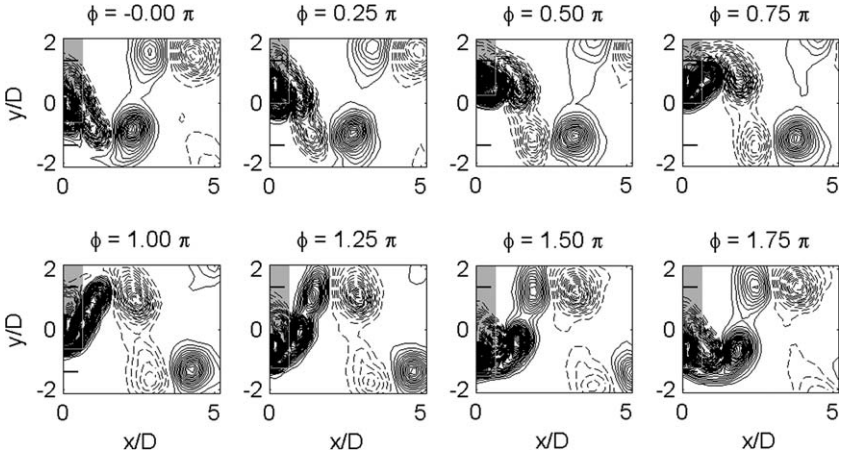

Fig. 12. Phase-averaged vorticity for case 18.

The large amount of DPIV/T data that was obtained in this study cannot all be included in this paper. Therefore, DPIT/V data is only shown for those cases specifically referred to in the discussion. The full results of these experiments are available in [24].

Contour plots of the phase-averaged normalized vorticity, $\omega D/U$, are shown for cases 13 (Fig. 7), 14 (Fig. 8), 17 (Fig. 10), 18 (Fig. 12), 20 (Fig. 13), 22 (Fig. 15), and 23 (Fig. 16). For each of these cases, 16 bins were used for the phase averaging, and every other phase is shown in the plot. Positive contours are indicated by solid lines, and negative contours are shown as dashed lines. The minimum contour levels are ± 0.2, and the contour spacing is also 0.2.

For cases 14 (Fig. 9), 17 (Fig. 11), 20 (Fig. 14) and 23 (Fig. 17), velocity vector fields with superimposed contours of normalized temperature,

$$\frac{T - T_\infty}{T_{\text{surf}} - T_\infty},$$

are also shown. The minimum normalized temperature contours are 0.015, and the contour spacing is 0.01.

4. Discussion

4.1. Synchronization with the Strouhal frequency and its harmonics

For small amplitudes, heat transfer is significantly enhanced by oscillations near the Strouhal frequency and its harmonics, as is highlighted in Fig. 18. Curves of $(Re/Re_0)^{1/2}$ are included for comparison to the expected increase in heat transfer if the effect of oscillations is due only to the increase in the effective speed of the flow. The effective speed is defined as the magnitude of the vector sum of the freestream flow and the root-mean-square of the oscillation velocity [15]. At the smallest amplitudes considered, the heat transfer coefficient is significantly enhanced near oscillation frequencies of 1 and 3 times the

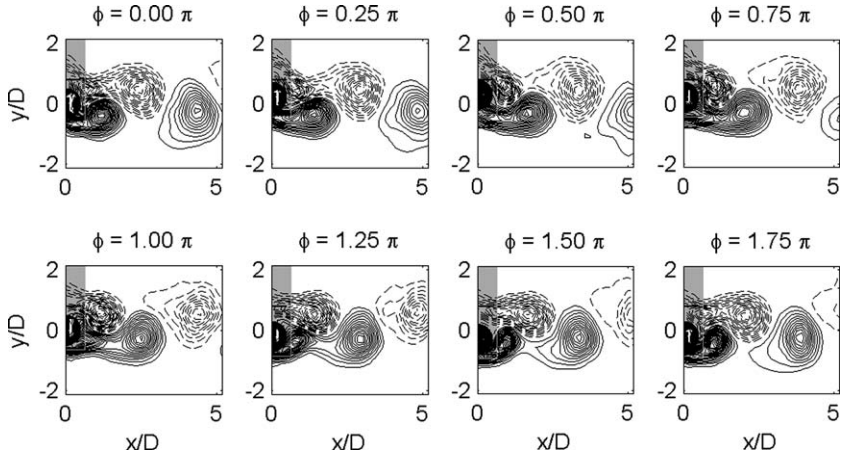

Fig. 13. Phase-averaged vorticity for case 20.

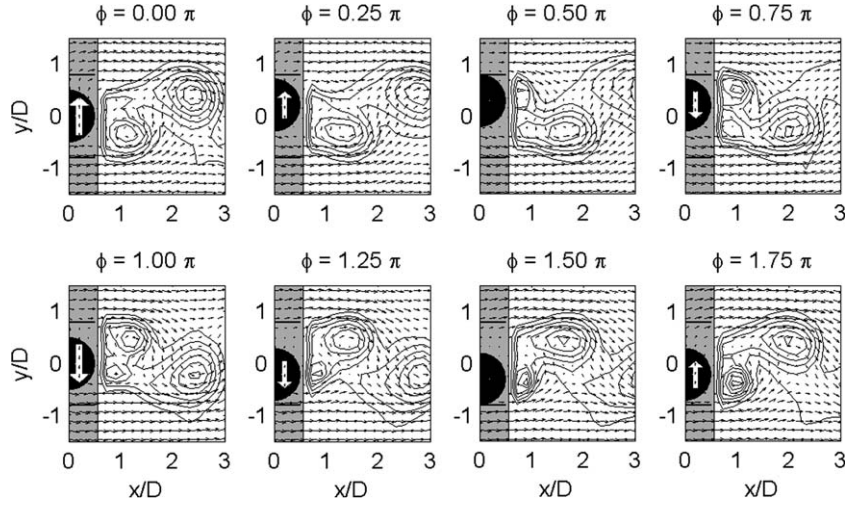

Fig. 14. Phase-averaged velocity and temperature for case 20.

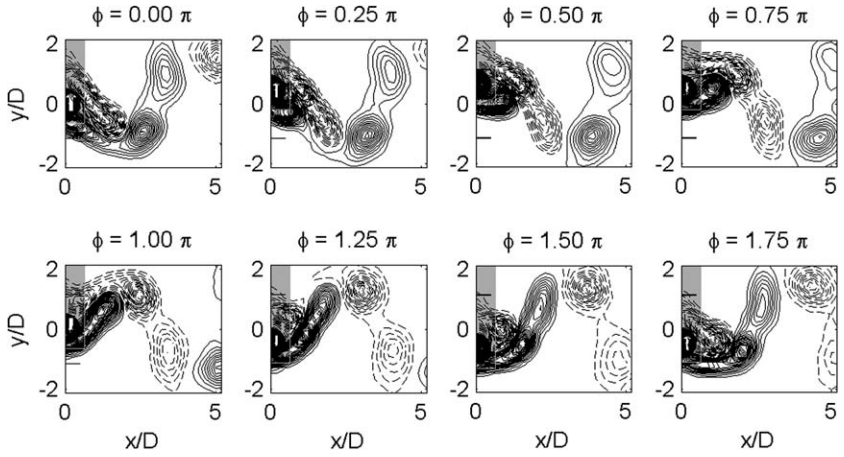

Fig. 15. Phase-averaged vorticity for case 22.

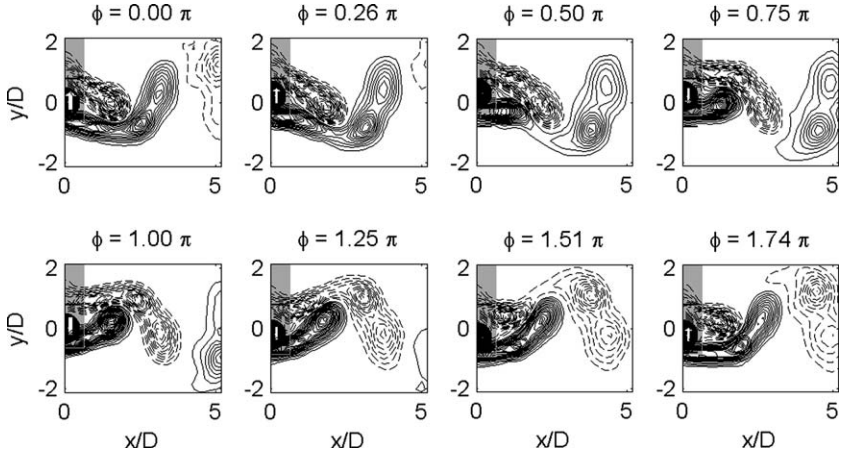

Fig. 16. Phase-averaged vorticity for case 23.

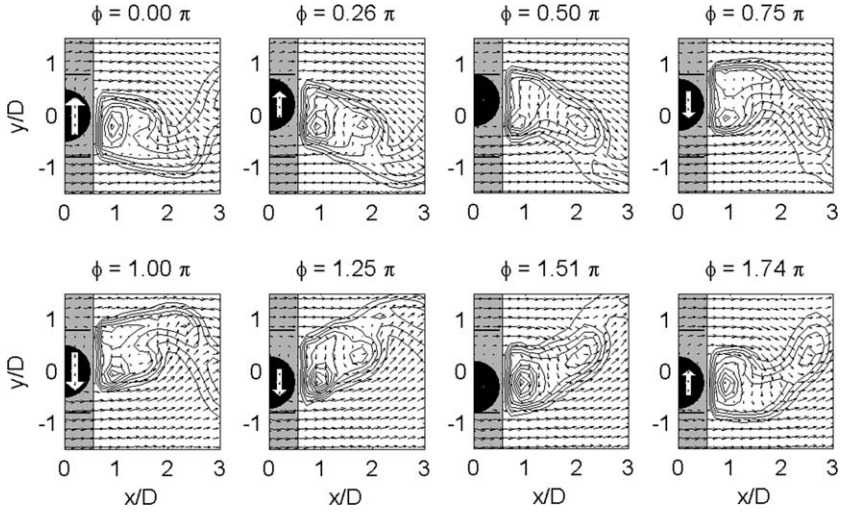

Fig. 17. Phase-averaged velocity and temperature for case 23.

Strouhal frequency. There is also minor heat transfer enhancement at $\frac{1}{3}$ and $\frac{2}{3}$ of the Strouhal frequency. For amplitude ratios greater than about 0.2, heat transfer is also enhanced near 2 times the Strouhal frequency. These effects persist up to amplitude ratios of about 0.4–0.5, as can be seen in Fig. 4. For each of the heat transfer peaks

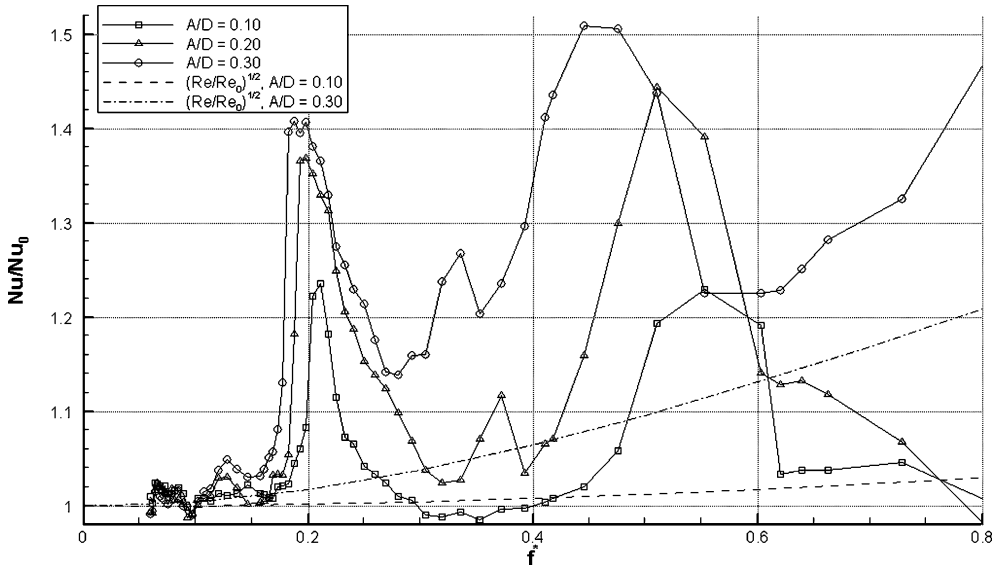

Fig. 18. Normalized heat transfer coefficient as a function of non-dimensional oscillation frequency.

associated with Strouhal frequency harmonics $f^* \geqslant St$, the non-dimensional frequency at which the peak occurs shifts toward lower frequency as the amplitude increases. The reason for this shifting is not known.

The existence of harmonic peaks is consistent with the work of other authors. The range of amplitude ratios and non-dimensional frequencies in the cases of interest are most comparable with the data of Park and Gharib [15]. While Park and Gharib do not have cases at this exact Reynolds number, the observed trends in the data are very similar. The only significant disagreement pertains to the low-frequency enhanced heat transfer cases. At some Reynolds numbers and some amplitude ratios, Park and Gharib found evidence of enhanced heat transfer at $\frac{1}{2}St$. Park and Gharib did not find any evidence of enhanced heat transfer at $\frac{1}{3}St$ or $\frac{2}{3}St$. However, the correspondence between the $2P + 2S$ wake mode and the $\frac{1}{3}St$ harmonic suggests that the present data is more consistent with real fluid phenomena.

4.2. Formation length

Park and Gharib [15] suggested that the vortex formation length, λ_f, significantly affects the heat transfer coefficient. The vortex formation length in turn depends on the oscillation conditions. According to Park and Gharib, for highly synchronized cases the wake vortices form close to the cylinder base and are therefore effective at removing hot fluid from the base region. For cases that are not strongly synchronized, the vortex roll-up process occurs far downstream of the cylinder, and the resulting heat transfer is near that of the non-oscillating cylinder. In order to compare with Park and Gharib's results, the formation length was determined for all cases in which the wake consists only of single, not paired, vortices.

The formation length was determined in two different ways. The first method is that used by Park and Gharib. They defined the formation length as the distance from the cylinder to the end of the wake bubble, or closed wake, in the mean velocity field. This location was identified using the critical point analysis of Perry and Fairlie [28]. For two-dimensional, incompressible flow only one of the invariants used by Perry and Fairlie, defined for the mean velocity field as

$$Q \equiv \det(\nabla \vec{u}_{\text{mean}}),$$

can take on a non-zero value. This quantity can be defined at each point in the flow where velocity data exists. If $Q > 0$ at a particular point, fluid at that point is undergoing rotation and is in the neighborhood of a center. Values of $Q < 0$ indicate that the point is in a saddle region. For this experiment, the quantity Q was computed at each point for which velocity data existed along a line located slightly off of the mean centerline of the cylinder ($y/D = -0.14$). An off-center line was chosen because on the centerline $Q = 0$ due to symmetry. Along this line, fluid inside the wake bubble is in the neighborhood of a center so $Q > 0$, while the end of the wake bubble is a saddle region where $Q < 0$. The formation length was therefore taken to be the streamwise distance from the cylinder base to the first point on this line with a value of $Q < 0$.

The second method used to determine the formation length was based upon the rms vorticity field. The formation length was defined as the streamwise distance from the cylinder base to the location of the peak rms vorticity on the same line. These definitions for the formation length generally agree with each other for wakes consisting of only single vortices.

Normalized heat transfer coefficients are plotted versus formation length in Fig. 19. The horizontal error bar

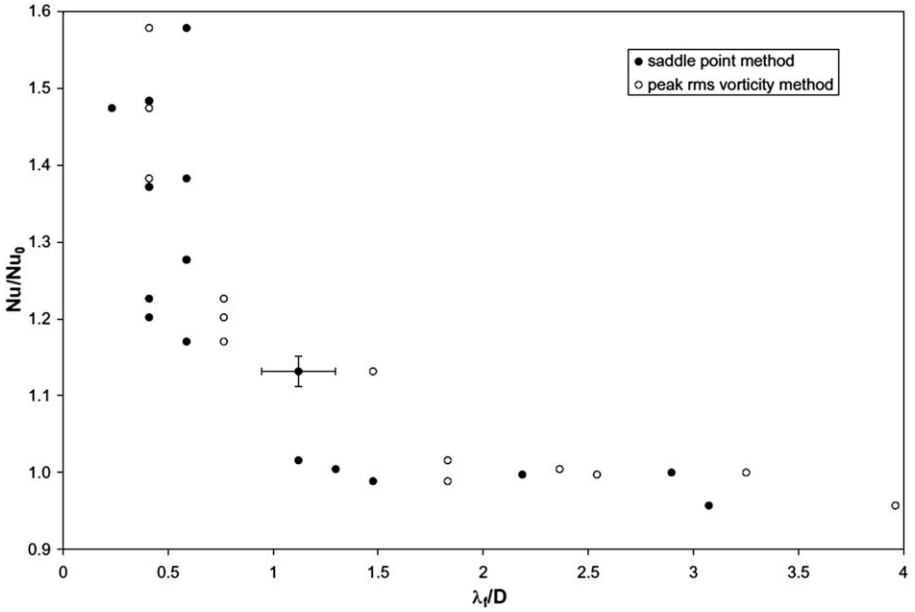

Fig. 19. Normalized heat transfer coefficient versus formation length for all cases consisting of only single vortices.

corresponds to the DPIV grid spacing, and the vertical error bars are due to the uncertainty in the measured heat transfer coefficient.

The present data supports Park and Gharib's conclusion that short formation length corresponds to enhanced heat transfer. The large number of cases in the present study, however, clarifies the relationship. While Park and Gharib's data was consistent with a linear relationship between these two factors, the present data indicates that some type of threshold effect occurs. For $\lambda_f/D > \sim 1.5$, there is no significant change in Nu/Nu_0 for different formation lengths. For $\lambda_f/D < \sim 1.5$, there is significant heat transfer enhancement, but the value of Nu/Nu_0 varies widely over a small range of formation lengths. This suggests that formation length is not the only factor that determines the heat transfer coefficient. It appears that a short formation length is necessary for significant heat transfer enhancement, but the magnitude of the enhancement is determined by other details of the wake structure.

4.3. Wake mode

The wake mode also appears to play a significant role in determining the heat transfer coefficient. The wake mode boundaries identified by Williamson and Roshko [3] are superimposed on the contour plots of normalized Nusselt number in Fig. 4. There is clearly a connection between wake mode boundaries and features of the contour plots. The $2S/2P$ boundary, near $1/f^* = 5.5$, corresponds to a region of steep gradient in the Nusselt number. At low frequency, it appears that there may be enhanced heat transfer in the $2P + 2S$ mode. At the highest non-dimensional frequencies observed, the contours of Nu/Nu_0 have a change in the sign of their slope for amplitude ratios between 0.7 and 0.9. While this does not correspond exactly to a wake mode boundary identified by Williamson and Roshko, it is very near the $C(2S)/C(P + S)$ boundary. Given that the exact position of the wake mode boundaries is known to vary with Reynolds number, it is likely that this slope change of the contours is related to a wake mode boundary.

The "turbulence effect" referred to by Cheng et al. [13] does not appear in the current data. Rather, the region of the parameter space in which this supposed effect was observed ($1/f^* < \sim 4$, $0.314 \leqslant A/D \leqslant 0.628$) is dominated by the third harmonic of the Strouhal frequency and the transition from a $2S$ to a $C(2S)$ wake mode. At the time of the Cheng et al. study, these wake phenomena were not known to affect the heat transfer, so the observed heat transfer enhancement was attributed to an assumed new effect. The wake mode and harmonic effects identified in the current data eliminate the need for a turbulence effect to explain the Cheng et al. data.

The wake mode for each DPIT/V case was identified using the phase-averaged vorticity field. The observed modes are tabulated in Table 1. In general, the wake modes agree well with the modes expected based upon the Williamson and Roshko [3] boundaries and the features of Fig. 4. In a few low-frequency cases, the observed wake structures differed from those reported by Williamson and Roshko [3], but this has no affect on the implications of the data. The reasons for the disagreement in wake modes are beyond the scope of this paper.

The wake structure revealed by the DPIT/V data explains why the heat transfer coefficient depends so strongly on wake mode. The most striking example of this dependence is the abrupt change in heat transfer coefficient across the $2S/2P$ boundary. Comparing case 20 ($2S$ mode;

Figs. 13 and 14) with case 23 (2*P* mode; Figs. 16 and 17), the role of the vortex formation process in affecting heat transfer is identifiable. Entrainment in the near-wake is very different for the two modes, as illustrated in the velocity and temperature field plots. For the 2*S* case, entrainment occurs between each successive vortex close to the cylinder base. In the 2*P* case, the extended shear layers—consisting of closely spaced forming vortices with the same sense of rotation—shift the entrainment further downstream, so the cool freestream fluid has less impact on the cylinder base region.

This is related to Park and Gharib's [15] formation length idea. The 2*P* mode always has extended shear layers, so vortices always detach from the shear layer farther downstream in the 2*P* mode than in the 2*S* mode. However, this is not the complete story. Unlike the wake of a non-oscillating cylinder, where the majority of the roll-up of vorticity occurs in a compact region located well downstream of the cylinder, in the 2*P* shear layers, the vortices begin to roll-up very close to the cylinder. For both the 2*S* and 2*P* roll-up processes, the vortices begin to roll-up at about the same downstream position, but they achieve very different maximum circulation values at very different locations. For the 2*S* case, each vortex remains close to the cylinder base for almost half of the oscillation cycle, resulting in high circulation at that location and a relatively large separation between vortices. This leads to entrainment of freestream fluid to the base region. For the 2*P* case, though each vortex begins to roll-up close to the cylinder, no vortex remains near the cylinder base as it grows. Instead, each vortex moves downstream as it grows, generating a series of closely spaced vortices that do not entrain a large amount of fluid. Most of the entrainment done by the vortices is farther downstream and is therefore ineffective at cooling the cylinder base region.

4.4. Streamwise spacing between vortices

The importance of streamwise spacing between vortices with the same sense of rotation was mentioned in the comparison of the 2*S* and 2*P* wake modes. This spacing is also found to be important in determining heat transfer for cases with the same wake mode.

A comparison of cases 14, 17 and 20 (Figs. 8 and 9; Figs. 10 and 11; Figs. 13 and 14) reveals that the spacing between shed vortices plays a role in determining the heat transfer in the 2*S* mode. The vortex spacing is a function of the vortex convective speed and the vortex shedding frequency, which in synchronized cases is equal to the oscillation frequency. While the formation process of the vortices prior to pinch-off appears almost identical for these three cases, the spacing of the shed vortices differs considerably. In these three cases, larger vortex spacing corresponds to higher heat transfer enhancement.

The heat transfer coefficient depends on the ability of the forming vortices to entrain freestream temperature fluid into the cylinder base region. A nearby vortex with the same sense of rotation would reduce the entrainment of outer flow fluid at the downstream side of the forming vortex by inducing a velocity directed away from the centerline. Fig. 9 (case 14), Fig. 11 (case 17) and Fig. 14 (case 20) demonstrate this. It is evident that larger vortex spacing corresponds to more entrainment of freestream fluid by the near-wake. This entrainment has the effect of bending the temperature contours, thereby creating a steeper temperature gradient in the cylinder base region. This results in a higher local heat transfer coefficient for the cylinder base. A similar effect may exist for other modes consisting of single vortices, but an insufficient number of cases were investigated in these modes in order to make that determination.

4.5. Transverse velocity

Over a significant portion of the parameter space investigated, mainly away from Strouhal frequency harmonics and wake mode boundaries, the contours of constant Nu/Nu_0 in Fig. 4 appear to be well described by straight lines that pass through the origin. In the $(1/f^*, A/D)$-plane, these rays are lines of constant peak transverse velocity for the cylinder. Since the cylinder motion is sinusoidal, the root-mean-square (rms) transverse velocity equals $\frac{1}{\sqrt{2}}$ times the peak transverse velocity, so

$$\frac{V_{\mathrm{rms}}}{U} = \sqrt{2}\pi f^* \frac{A}{D}.$$

The normalized heat transfer coefficient is plotted versus the non-dimensional transverse velocity in Fig. 20a. While there is significant scatter for $V_{\mathrm{rms}}/U < 1$, the data appears to partially collapse for larger values of V_{rms}/U. The data appears to follow two main curves, with a small number of data points falling between the two curves.

The bifurcation in the data was examined by excluding data points associated with harmonics of the Strouhal frequency and identifying the wake mode of each remaining data point. For purposes of understanding this bifurcation, the wake mode boundaries are assumed to be the previously described features of the contour plot in Fig. 4. The results of this sorting are shown in Fig. 20b. It is apparent that the two curves of data points correspond to two different types of wake modes. This indicates that, within a given wake mode, transverse velocity determines the heat transfer coefficient.

Transverse velocity can affect heat transfer enhancement in two ways. First, it can increase the circulation of the forming vortices by increasing the vorticity flux in the shear layers. Second, it can allow the vortices to affect a larger portion of the cylinder surface area.

The vorticity flux past a point on a boundary is a function of the outer flow velocity relative to that boundary. For an oscillating cylinder, the cylinder transverse velocity can be a significant source of vorticity flux. This suggests that for cases with the same basic wake structure, higher transverse velocity should lead to higher circulation in the wake vortices. For a particular vortex roll-up process

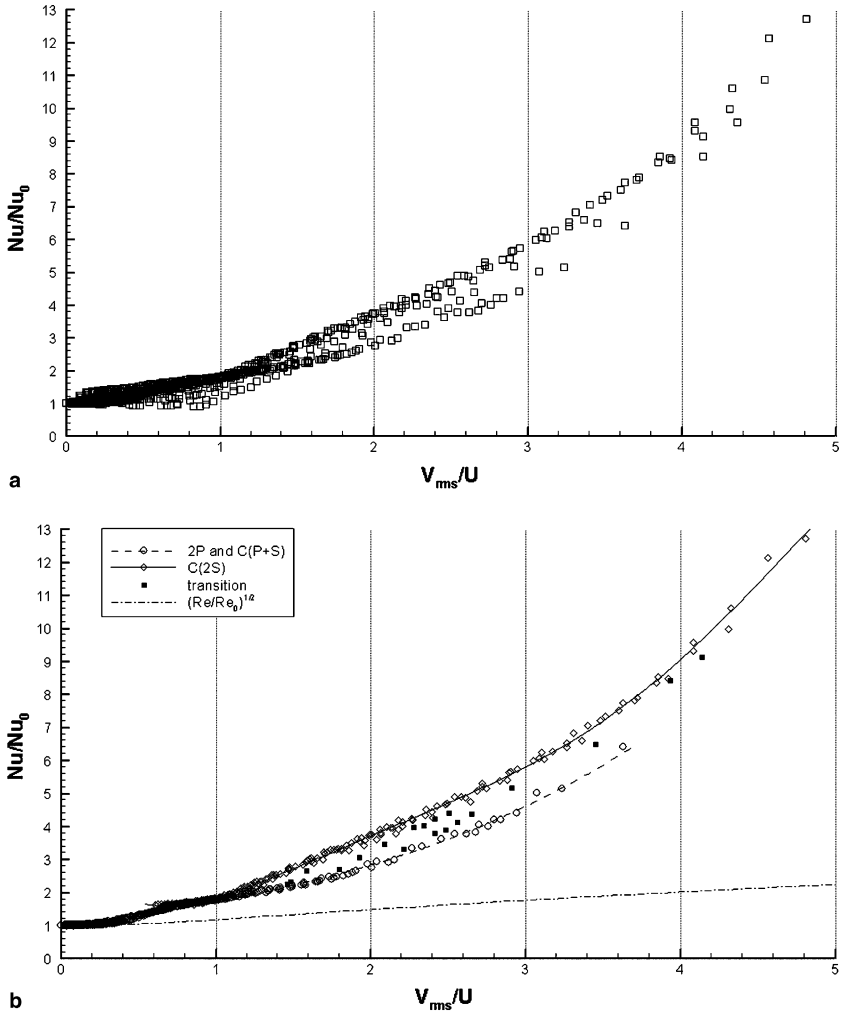

Fig. 20. Normalized Nusselt number versus rms transverse velocity (a) for all cases (b) with wake mode identified and frequency synchronizations removed.

and distance, the circulation of the vortices is expected to determine the entrainment and mixing in the cylinder base region and should therefore determine the heat transfer enhancement.

The second effect of high transverse velocity is to expose a larger portion of the cylinder surface area to the high velocities and mixed fluid generated by forming vortices. As the cylinder moves transversely, the wake turns so as to be somewhat aligned with the instantaneous direction of the flow relative to the cylinder. The higher the transverse velocity, the greater the angle through which the wake turns. For conditions where the vortices roll-up close to the cylinder, heat transfer is primarily enhanced for the cylinder base region due to the proximity of the vortices. By moving the vortices over a larger portion of the cylinder base, higher transverse velocities should result in increased heat transfer enhancement for a particular wake mode.

These two effects can be seen in cases 13, 18, 22 and 23 (Figs. 7, 12, 15 and 16). These are all $2P$ wakes with the leading vortex in each pair containing approximately twice the circulation of the trailing member of the pair. The four cases have different transverse velocities, and the heat transfer coefficient increases with increasing transverse velocity.

For each case, the circulation

$$\Gamma = \oint \vec{u} \cdot \mathrm{d}\vec{s} = \int\int \omega \,\mathrm{d}A$$

of each pinched-off vortex was determined by summing the vorticity inside a contour at $\omega D/U = \pm 0.2$, and multiplying by the area of the grid elements. Circulation is normalized as Γ/UD. These results are shown in Fig. 21. As expected, the circulation of the vortices increases with increasing transverse velocity. The error bars indicate the difference between the absolute value of the measured circulation of the positive and negative vortices.

Fig. 21 also shows the maximum angle, over the course of a cylinder oscillation cycle, between the freestream direction and a line connecting the center of the cylinder to the lead vortex in a pair while it was immediately adjacent to the cylinder. This angle, η, is defined as positive towards the side of the cylinder with the shear layer of opposite

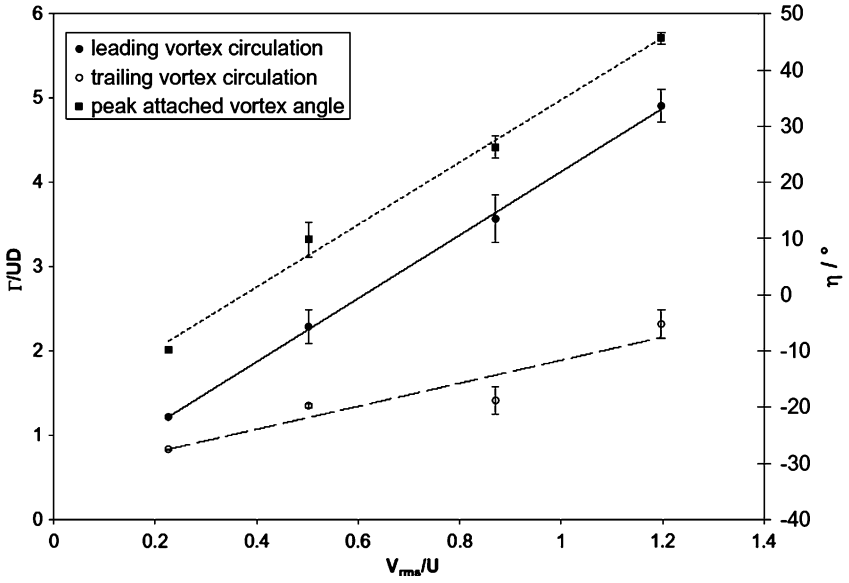

Fig. 21. Normalized circulation and vortex shedding angle versus normalized rms transverse velocity for cases 13, 18, 22 and 23.

sense of rotation as the vortex. Therefore, a negative η indicates that the vortex remains on its original side of the cylinder while near the cylinder, and a positive η indicates that the vortex moves around the cylinder to the other side. Clearly, high transverse velocity causes the vortices to move over a large portion of the cylinder surface area.

5. Conclusion

The details of an investigation into the effects of transverse oscillations on the heat transfer from a circular cylinder have been presented. Based upon the results of this investigation, several conclusions can be drawn.

First, heat transfer is significantly enhanced by small amplitude oscillations at frequencies near the Strouhal frequency and its harmonics. While previous authors have observed this heat transfer enhancement, it was shown for the first time that this effect is limited to amplitude ratios less than about 0.5. Shortening of the formation length in the wake at these conditions explains this effect. This mechanism was first proposed by Park and Gharib [15], and the present study indicates that short formation length is only one of several factors influencing heat transfer coefficient.

Second, the details of the vortex roll-up process in the cylinder wake were found to affect the heat transfer coefficient significantly. The wake mode is directly related to the heat transfer coefficient. Many features in the contour plot of normalized heat transfer coefficient correspond to known wake mode boundaries. DPIT/V data revealed that the trajectories of the vortices during roll-up govern the cylinder heat transfer coefficient by determining the location at which entrainment of freestream fluid occurs. Also, the streamwise spacing of shed vortices was correlated with heat transfer coefficient for the 2*S* mode. The physical mechanism resulting in this correlation is the effect of streamwise spacing on the entrainment of freestream temperature fluid by the forming vortices.

Finally, the transverse cylinder velocity was shown to play a significant role in determining the heat transfer coefficient. Within a particular wake mode and away from effects associated with the Strouhal frequency, the transverse cylinder velocity is the primary factor responsible for variations in heat transfer coefficient. Two mechanisms were identified through which the transverse cylinder velocity affects the heat transfer. First, the cylinder's transverse oscillations produce additional vorticity, which rolls up in the wake. The transverse velocity is therefore a factor in determining the circulation of the wake vortices. For a fixed wake structure, the circulation of the vortices determines their effectiveness at enhancing heat transfer. Second, high transverse velocity moves the vortices, which are responsible for the heat transfer enhancement, over a larger portion of the cylinder base by turning the wake with respect to the freestream.

While these experiments were carried out at low Reynolds number, it is possible that these mechanisms of heat transfer enhancement may exist at high Reynolds number as well. It would therefore be of great value to conduct similar experiments at high Reynolds number.

Acknowledgements

This work was supported by the US National Science Foundation under grant CTS 9903346. The first author would also like to thank the National Defense Science and Engineering Graduate Fellowship program for financial support.

References

[1] S. Taneda, Experimental investigation of the wakes behind cylinders and plates at low Reynolds numbers, J. Phys. Soc. Jpn. 11 (3) (1956) 302–307.

[2] C. Norberg, An experimental investigation of the flow around a circular-cylinder—influence of aspect ratio, J. Fluid Mech. 258 (1994) 287–316.

[3] C.H.K. Williamson, A. Roshko, Vortex formation in the wake of an oscillating cylinder, J. Fluids Struct. 2 (1988) 355–381.

[4] F.P. Incropera, D.P. Dewitt, Fundamentals of Heat and Mass Transfer, fourth ed., John Wiley and Sons, New York, 1996, pp. 366–373.

[5] A. Zhukauskas, Heat transfer from tubes in cross flow, in: J.P. Hartnett, T.F.J. Irvine (Eds.), Advances in Heat Transfer, vol. 8, Academic Press, New York, 1972, pp. 116–133.

[6] A.F. Mills, Average Nusselt numbers for external flows, J. Heat Transfer—Trans. ASME 101 (4) (1979) 734–735.

[7] V.T. Morgan, The overall convective heat transfer from smooth circular cylinders, in: J.P. Hertnett, T.F. Irvine Jr. (Eds.), Advances in Heat Transfer, vol. 11, Academic Press, New York, 1975, pp. 199–264.

[8] A. Quarmby, A.A.M. Alfakhri, Effect of finite length on forced-convection heat-transfer from cylinders, Int. J. Heat Mass Transfer 23 (4) (1980) 463–469.

[9] B.H. Chang, A.F. Mills, Effect of aspect ratio on forced convection heat transfer from cylinders, Int. J. Heat Mass Transfer 47 (6–7) (2004) 1289–1296.

[10] K. Sreenivasan, A. Ramachandran, Effect of vibration on heat transfer from a horizontal cylinder to a normal air stream, Int. J. Heat Mass Transfer 3 (1961) 60–67.

[11] S.P. Kezios, K.V. Prasanna, Effect of vibration on heat transfer from a cylinder in normal flow, 66-WA/HT-43, ASME Paper No., 1966.

[12] U.C. Saxena, A.D.K. Laird, Heat-transfer from a cylinder oscillating in a cross-flow, J. Heat Transfer—Trans. ASME 100 (4) (1978) 684–689.

[13] C.H. Cheng, H.N. Chen, W. Aung, Experimental study of the effect of transverse oscillation on convection heat transfer from a circular cylinder, J. Heat Transfer—Trans. ASME 119 (3) (1997) 474–482.

[14] C. Gau, J.M. Wu, C.Y. Liang, Heat transfer enhancement and vortex flow structure over a heated cylinder oscillating in the crossflow direction, J. Heat Transfer—Trans. ASME 121 (4) (1999) 789–795.

[15] H.G. Park, M. Gharib, Experimental study of heat convection from stationary and oscillating circular cylinder in cross flow, J. Heat Transfer—Trans. ASME 123 (1) (2001) 51–62.

[16] C.E. Willert, M. Gharib, Digital particle image velocimetry, Exp. Fluids 10 (4) (1991) 181–193.

[17] S.P. McKenna, W.R. McGillis, Performance of digital image velocimetry processing techniques, Exp. Fluids 32 (1) (2002) 106–115.

[18] M. Parsley, The Hallcrest Handbook of Thermochromic Liquid Crystal Technology Ed., Hallcrest, Glenview, IL, 1991.

[19] E.J. Klein, Application of liquid crystal to boundary layer flow visualization, 68-376, AIAA Paper No., 1968.

[20] H.S. Rhee, J.R. Koseff, R.L. Street, Flow visualization of a recirculating flow by rheoscopic liquid and liquid-crystal techniques, Exp. Fluids 2 (2) (1984) 57–64.

[21] D. Dabiri, M. Gharib, Digital particle image thermometry—the method and implementation, Exp. Fluids 11 (2–3) (1991) 77–86.

[22] H.G. Park, D. Dabiri, M. Gharib, Digital particle image velocimetry/thermometry and application to the wake of a heated circular cylinder, Exp. Fluids 30 (3) (2001) 327–338.

[23] H.G. Park, A study of heat transfer processes in the wake of a stationary and oscillating circular cylinder using digital particle image velocimetry/thermometry, Ph.D. thesis, California Institute of Technology, Pasadena, CA, 1998.

[24] T.S. Pottebaum, The relationship between near-wake structure and heat transfer for an oscillating circular cylinder in cross-flow, Ph.D. thesis, California Institute of Technology, Pasadena, CA, 2003.

[25] D.R. Sabatino, T.J. Praisner, C.R. Smith, A high-accuracy calibration technique for thermochromic liquid crystal temperature measurements, Exp. Fluids 28 (6) (2000) 497–505.

[26] C. Norberg, Fluctuating lift on a circular cylinder: review and new measurements, J. Fluids Struct. 17 (1) (2003) 57–96.

[27] C.H.K. Williamson, Vortex dynamics in the cylinder wake, Ann. Rev. Fluid Mech. 28 (1996) 477–539.

[28] A.E. Perry, B.D. Fairlie, Critical points in flow patterns, Adv. Geophys. B 18 (1974) 299–315.